A Low-Cost Printed Circuit Board Design for External Force Measuring in Robotic Applications

H. Meneses[a], V. Jarquin,[b], Y. Miranda [c], C. Cordero[d], N. Delgado[e], K. Vargas[f] and F. Ruíz[g]

Instituto de Investigaciones en Ingeniería, Facultad de Ingeniería, Universidad de Costa Rica, 11501-2060, San José, Costa Rica
{*helber.meneses, valeria.jarquin, yehohnathan.miranda, carlos.corderoretana,*

Keywords: Force Sensing, Impedance Control, Printed Circuit Board, Strain Gauge, Wheatstone Bridge.

Abstract: This paper presents a low-cost printed circuit board designed to measure external forces in several robotics applications. Its operating principle is based on capturing electrical resistance change coming from strain gauges attached to deformable beams in elastic force-torque sensors. This system offers great flexibility because users can adjust up to 8 Wheatstone bridge circuit in different configurations depending on their needs, their parameters as offset and amplification gain can easily be configured and the assembly process is intended to be fast using a pick-and-place machine and a soldering oven.

1 INTRODUCTION

In the last decade the interest to bring out robots or autonomous systems form factories has risen due to their capacity to develop repetitive tasks (Prabakaran et al., 2018), to execute dangerous jobs made in hazardous environments (Wong et al., 2018) or to support elderly people in daily activities (Oda et al., 2010).

The main limitations to achieve this goal are based on their economic cost and their capacities to be safe for the objects and people in the environment (Kim et al., 2016). Some works have dealt with the last issue incorporating force control approaches as the well known impedance or admittance control (Calanca et al., 2016) based on force-torque sensors located in particular robot joints (Dietrich et al., 2016; Kim et al., 2016; Kim et al., 2014; Bussmann et al., 2018; Iskandar et al., 2019; Sentis et al., 2013; Nozawa et al., 2011), wrapping the robot in a kind of skin made up of a large number of pressure sensors (Armleder et al., 2022; Cheng et al., 2019; Dean et al., 2019; Mittendorfer, 2012) or attaching a 6 degree of freedom (DoF) force-torque sensor to a rigid robot shell in one point (Kollmitz et al., 2018) or to a rigid body part (Frémy et al., 2014; Oda et al., 2010; Aguirre-Ollinger and Yu, 2021).

In literature, one of the preferred technologies to build force-torque sensors is based on strain gauges that capture the mechanical deformation of elastic material. For instance, the works presented by (Chen et al., 2015; Yuan et al., 2015; Valizadeh et al., 2015; Lin et al., 2019; Sun et al., 2013; Phan et al., 2018; Kebede et al., 2019) analysed the design and implementation of force-torque sensor with up to eight Wheatstone bridge in quarter, half, full bridge configurations or a mix of them.

The main reasons to employ this piezo-resistive sensor has attractive qualities, namely, high measurement accuracy and it is suitable for static or quasi-static measurements (Chen et al., 2015), and temperature compensation is possibly achieved using Wheatstone bridge circuits (Templeman et al., 2020).

Until now, it is of our knowledge in literature, that there is not a complete low-cost printer circuit board design that shows the whole configuration to sense external forces due to mechanical strain changes in elastic bodies, an therefore we proposed a whole description of each stage and the components required to guarantee an optimal performance and flexibility to select different Wheatstone bridge circuit configurations depending on the user requirements.

[a] https://orcid.org/0000-0001-7119-3100
[b] https://orcid.org/0009-0007-2339-3678
[c] https://orcid.org/0009-0001-5842-0097
[d] https://orcid.org/0009-0007-9435-7922
[e] https://orcid.org/0009-0006-4099-8671
[f] https://orcid.org/0009-0009-1958-7554
[g] https://orcid.org/0000-0001-8563-4341

Meneses, H., Jarquin, V., Miranda, Y., Cordero, C., Delgado, N., Vargas, K. and Ruíz, F.
A Low-Cost Printed Circuit Board Design for External Force Measuring in Robotic Applications.
DOI: 10.5220/0012238800003543
In *Proceedings of the 20th International Conference on Informatics in Control, Automation and Robotics (ICINCO 2023) - Volume 2*, pages 211-218
ISBN: 978-989-758-670-5; ISSN: 2184-2809

The paper is organized as follows: Section 2 presents the functionalities of the printed circuit board, Section 3 shows the printed circuit board design, Section 4 shows the economic cost, Section 5 presents a comparison with some commercial acquisition boards and finally, Section 6 presents the main results of the printed circuit board design.

2 SYSTEM CONFIGURATION

The printed circuit board (PCB) is composed by four main blocks as can be seen in Fig. 1. The power supply circuits responsible to transfer required energy to achieve the different functionalities and configurations, the Wheatstone bridge circuits used to capture the resistance change due to the mechanical deformation on the elastic parts, the amplification system in charge of amplifying voltage signal coming from Wheatstone bridge in order to have a suitable reading in the analog to digital converters and the microcontroller responsible for signals processing to estimate external force values.

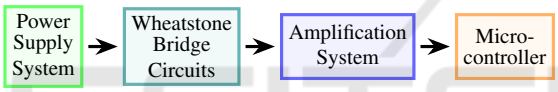

Figure 1: Printed circuit board system configuration.

2.1 Power Supply System

The power supply system is composed by three stages. The first one shown in Fig. 2 is responsible for capturing the energy from a 12 V battery or a similar system and it has an inverse polarity protection based on a P-Channel MOSFET to avoid a damage in the rest of the system due to a wrong user connection. A similar protection circuit is recommended by (Scrimizzi et al., 2016) because other solutions based on a diode entails higher power losses and a circuit protection based on a N-Channel MOSFET requires an additional driver circuit composed by a charge pump circuit and EMI filter. As it is mentioned by (ONSEMI, 2023), when a reverse polarity protection based on a P-Channel MOSFET is used, to turn on a P-Channel, the gate voltage needs to be lower than the source voltage by at least the threshold voltage specified by the manufacturer and this requirement is fulfilled with a right connection using the circuit shown in Fig. 2, but when the battery is reversely connected, the gate and source voltage are practically the same and therefore, the P-channel is turn off. Note, that there is a solder bridge jumper in parallel with a MOSFET transistor if the user decides to do not use that protections for any reason. Also, it can be seen several capacitors that deal with battery voltage changes and provide a low impedance path to high frequency noise coming from the battery voltage.

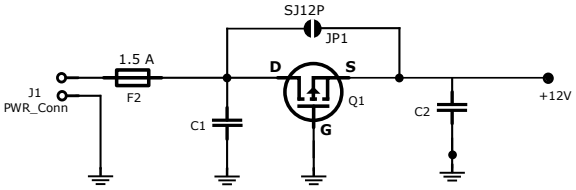

Figure 2: Main power system.

The second one is connected to the previous stage and it can be seen in Fig. 3. It is composed by a 9 V voltage regulator that supplies a 9 V constant voltage to the Wheatstone bridge in order to have a higher voltage due to the electrical resistance change in comparison to the obtained when the Wheatstone bridge is power to typical voltages values as 5 V or 3.3 V. Note, that it is also possible to use 12 V coming from the battery to power the Wheatstone bridge closing the solder bridge jumper located parallel to the 9 V voltage regulator. Moreover, in the output of the voltage regulator there is a diode to protect it in case of current coming from inverse direction. Also, the capacitors in this stage perform similar functions to those mentioned above: regulate voltage changes and filter high frequency noise. This stage also provides the required voltage level by the operational amplifier that will be shown further.

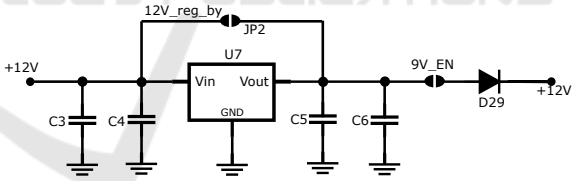

Figure 3: 9 V voltage regulator system.

The last stage of the power system is shown in Fig. 4. It is composed mainly by a 5 V voltage regulator whose power supply can come from 9 V voltage regulator or from 12 V battery. The output voltage of this regulator is employed to power the microcontroller STM32F407 Discovery as well as a 1.6 V reference voltage chip used by the amplification voltage system. The capacitors shown in this stage also execute the same functions of the capacitors mentioned above.

2.2 Wheatstone Bridge Circuits

The PCB has eight Wheatstone bridge circuits that can be implemented as quarter, half or full bridge configuration as it can be seen in Fig. 5 selecting prop-

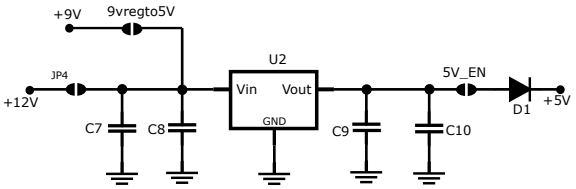

Figure 4: 5 V voltage regulator system.

erly the solder bridge jumpers *JP1*, *JP2*, *JP3*, *JP4*, *JPV1*, *JPV2*, *JPV3* and *JPV4*. Note that RV1, RV2, RV3, and RV4 are 50 Ω trimmers that are in series with either a strain gauge of typical values of 120 Ω or 350 Ω (*Gauge 1*, *Gauge 2*, *Gauge 3* or *Gauge 4*) or with a 100 Ω or 330 Ω resistor (*R1*, *R2*, *R3* or *R4*) and they allow to adjust an equal resistance on each Wheatstone bridge arm in order to have a null voltage generation when no force is applied.

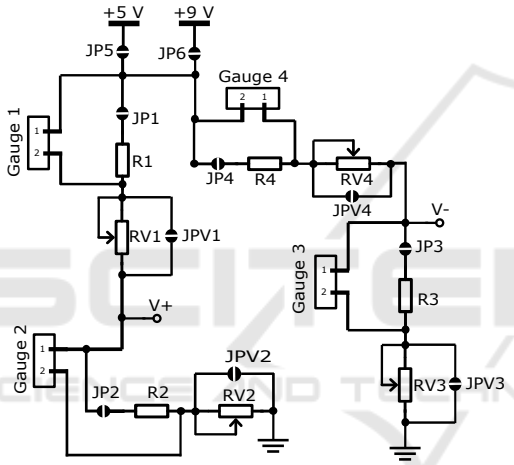

Figure 5: Wheatstone bridge.

The output voltage V_d coming from the Wheatstone bridge circuit is given by:

$$V_d = V+ - V- = Vcc \cdot \left(\frac{R_{2G}}{R_{1G}+R_{2G}} - \frac{R_{3G}}{R_{4G}+R_{3G}} \right) \quad (1)$$

where R_{iG} is the i-th strain gauge resistance (i = 1,2 on the right Wheatstone bridge arm and i = 3,4 on the left Wheatstone bridge arm) and V_{cc} could be either 9 V or 5 V as it is shown in Fig. 5. If $R_{2G} = R_{4G} = R_T$ and $R_{1G} = R_{3G} = R_C$, then:

$$V_d = V_+ - V_- = Vcc \cdot \left(\frac{R_T - R_C}{R_T + R_C} \right) \quad (2)$$

Note that $V_o > 0$ if $R_T > R_C$ and this happen when both strain gauges 2 and 4 or any of them operate in tension (resulting in increased resistance) and both strain gauges 1 and 3 or any of them operate in compression (resulting in decreased resistance). When the mechanical deformation happens in the inverse direction the voltage output is $V_o < 0$ and therefore, it is possible to have positive and negative voltage values according to the direction of the external force applied on the force-torque sensor.

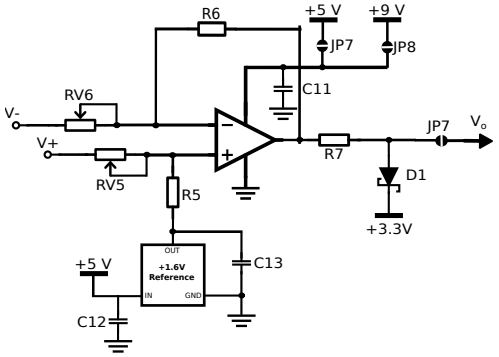

Figure 6: Voltage amplification system.

2.3 Voltage Amplification System

In order to have a better reading of the voltage signals coming from the Wheatstone bridge circuits, an operational amplifier with instrumentation characteristics was chosen as it can be seen in Fig. 6. For this PCB the TLV9154QDRQ1 was chosen. Among its main features, there is a typical bandwidth of 4.5 MHz, a slew rate of 21 V/ μs and a common-mode rejection ratio of 125 dB.

At it is shown in this figure, a 1.6 V voltage reference chip is required to get a voltage offset different from zero (1.6 V) as output of the amplification system.

Therefore, the voltage output V_o is given by:

$$V_o = \frac{R5}{RV5}\frac{\left(1+\frac{R6}{RV6}\right)}{\left(1+\frac{R5}{RV5}\right)}V_+ - \frac{R6}{RV6}V_- + \frac{\left(1+\frac{R6}{RV6}\right)}{\left(1+\frac{R5}{RV5}\right)}1.6 \quad (3)$$

Note that trimmers $RV5$ and $RV6$ are adjusted in such way that relation (4) is accomplished:

$$\frac{R6}{RV6} = \frac{R5}{RV5} \quad (4)$$

Therefore, the voltage output can be expressed as:

$$V_o = \frac{R6}{RV6}(V_+ - V_-) + 1.6 \quad (5)$$

where the term $\frac{R6}{RV6}$ represents the amplification gain.

3 PRINTED CIRCUIT BOARD DESIGN

The printed circuit board was designed using KiCad 7.0 which is an open source software developed for

electronics circuits design. It offers an schematic capture where electrical diagram is created as well as a PCB layout where the location of the different components is made and important characteristics as track width, via size, clearance, power and ground planes, and PCB layer stackup are defined.

3.1 PCB Layer Stackup

The general purpose of this printed circuit board is sending all the voltage signals to the analog to digital converts in an accurate and quickly way. A good practice to do that is through the use of impedance control which avoids distortion, attenuation and reflection of the signals and improves the reliability of the measurements that are performed within the PCB (Zhang et al., 2011).
For this design, the standard JLC04161H-7628 (https://jlcpcb.com/impedance) shown in Tab. 1 was chosen as an option for impedance control because it is a standard used for high data transmission applications (Circuits, 2020), as this case. This four layer configuration was also chosen because it allows connections between all the electrical components despite their large number.

Table 1: Dielectric Specifications LC04161H-7628 (https://jlcpcb.com/impedance).

Layer	Material	Tickness (mm)
L1	Outer Copper Weight, 1 oz A	0.0350
Prepreg	7628, RC 49%, 8.6 mil A	0.2104
L2	Inner Copper Weight A	0.0152
Core	1.1mm H/HOZ with copper A	1.0650
L3	Inner Copper Weight	0.0152
Prepreg	7628, RC 49%, 8.6 mil A	0.2104
L4	Outer Copper Weight, 1 oz	0.0350

A visual distribution of the layer stackup is shown in Fig. 7. In our case, L1 layer corresponds to the front copper layer where most of surface mounting device (SMD) components are positioned in order to facilitate the assembly process using a pick-and-place machine (P&P) and a soldering oven as it can be seen in Fig. 9. All the trimmers were selected as through-hole technology because they are cheaper than other technologies and they were mounted on this layer to facilitate their resistance adjustment. The strain gauge connectors are also mounting on this layer. L2 layer represents the ground plane, L3 layer the power planes which has the distributions of the different voltage level required by the PCB as it can be seen in Fig. 8. Layer L4 corresponds to the back copper layer which has the power connector, voltage regulators and few smd components as capacitors as it can be seen in Fig. 10.

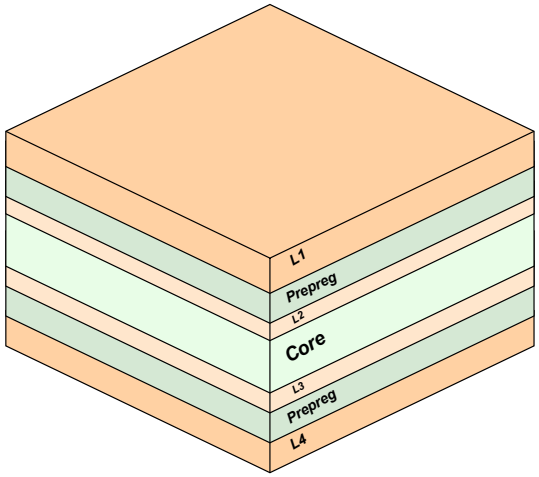

Figure 7: The JLC04161H-7628 (Standard) stackup offered by JLCPCB implemented in the PCB design.

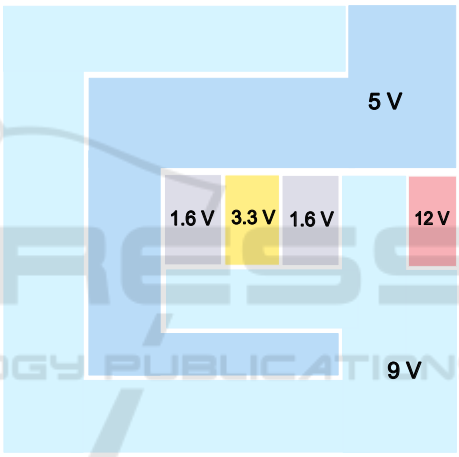

Figure 8: Power Plane Distribution.

3.2 Net Classes Configuration

In Kicad it is possible to define a set of nets that have the same parameters to route these nets and this is called as *Net Classes*. This is very useful to define the most important parameters for proper implementation of PCB traces. The parameters of these classes were defined as follows:

- Clearance: minimum values are used with an additional 30 % margin to provide a suitable margin, following the electrical spacing specified by the IPC 2221 standard (The Institute for Interconnecting and Packaging Electronic Circuits, 1998). Please note that these values are intended for uncoated external components (A6).
- Track Width: it was calculated by using the formula (6) specified in the IPC 2221 standard considering a temperature change of 10 degrees Celsius and the estimated current values shown in

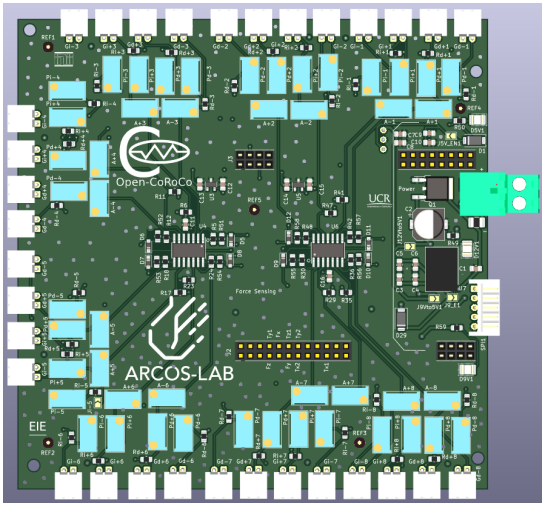

Figure 9: Components distribution on frontal layer.

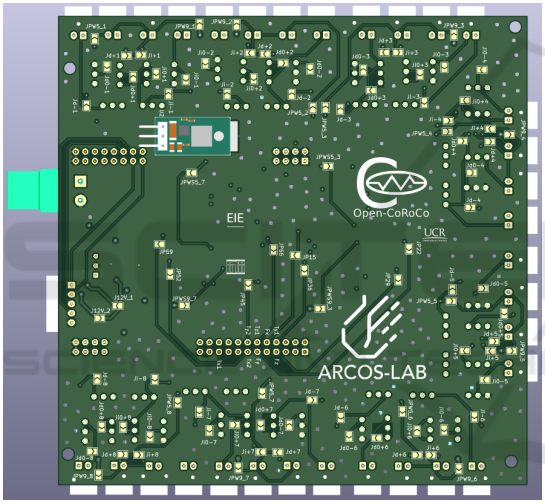

Figure 10: Components distribution on back layer.

Tab. 2 for the defined Net Classes. Note that *Analog_Signal* refers mainly to the current signals crossing the Wheatstone bridge circuits and the amplification voltage system, the *GND_Analog* refers to the current crossing the ground plane and the rest of Net Classes refer to the circulating current in a stage with an specific voltage level. The remaining variables for track width calculation were set according to the specifications outlined in the IPC 2221 standard (The Institute for Interconnecting and Packaging Electronic Circuits, 1998).

$$I = K \cdot \Delta T^{0.44} \cdot (W \cdot H)^{0.725} \quad (6)$$

- Via Hole: typically, it has the same value as the track width because the width of the track should always have a Via Hole of at least the same size to accommodate the track. A minimum value of 0.3 mm was set to minimize economic cost, considering the purchase options available by JLCPCB manufacturer. A large Via Hole size improves heat dissipation (Singh et al., 2019).
- Via Size: it is advisable to use a value twice the size of the Via Hole. For example, if a Via Hole of 0.3 mm is used, a Via Size of 0.6 mm ensures an annular ring of 0.15 mm (JLCPCB, 2023). This helps to minimize costs, considering the options available at JLCPCB manufacturer for instance.
- uVia Size: microvias that connect inner layers with outer layers maintain the same value as their corresponding Via Size. This is done to reduce costs.
- uVia Hole: microvias that connect inner layers with outer layers maintain the same value as their corresponding Via Hole. This is done to reduce economic cost.

Table 2: Current calculations for different Net Classes on the PCB.

Net Class	Current	Current + 30%
Analog_Signal	0.160 A	0.208 A
GND_Analog	1.673 A	2.391 A
Power_Analog_1.6V	0.012 A	0.0156 A
Power_Analog_12V	1.10 A	1.57 A
Power_Analog_3V	0.263 A	0.342 A
Power_Analog_5V	0.693 A	0.990 A
Power_Analog_9V	1.10 A	1.57 A

Consequently. the Net classes parameters defined in KiCad are shown in Tab. 3 and 4.

Table 3: NetClasses parameters used in PCB design according to the track requirements.

Net Class	Clearance	Track Width	Via Size
Default	0.16 mm	0.16 mm	0.6 mm
Analog_Signal	0.16 mm	0.16 mm	0.6 mm
GND_Analog	0.4 mm	1 mm	2 mm
Power_Analog_1.6V	0.16 mm	0.16 mm	0.6 mm
Power_Analog_12V	0.25 mm	0.56 mm	1.12 mm
Power_Analog_3V	0.16 mm	0.16 mm	0.6 mm
Power_Analog_5V	0.16 mm	0.3 mm	0.6 mm
Power_Analog_9V	0.25 mm	0.56 mm	1.12 mm

Table 4: NetClasses parameters used in PCB design according to the track requirements.

Net Class	Via Hole	uVia Size	uVia Hole
Default	0.3 mm	0.6 mm	0.3 mm
Analog_Signal	0.3 mm	0.6 mm	0.3 mm
GND_Analog	1 mm	2 mm	1 mm
Power_Analog_1.6V	0.3 mm	0.6 mm	0.3 mm
Power_Analog_12V	0.56 mm	1.12 mm	0.56 mm
Power_Analog_3V	0.3 mm	0.6 mm	0.3 mm
Power_Analog_5V	0.3 mm	0.6 mm	0.3 mm
Power_Analog_9V	0.56 mm	1.12 mm	0.56 mm

4 PCB ECONOMIC COST

The list of components used for the PCB design is shown in Tab. 5 and 6. It contains the part number of each component, its price, the type of assembly: through-hole (T-H) or SMD as well as the required quantity. The total estimated cost including the STM32F407 Discovery microcontroller was $62.75. The acronyms used in this list are: *Op Amps* for operational amplifiers, *G* for gauge, *P* for power, *R* for resistor, *T* for trimmer, *C* for capacitor and *V* for voltage.

Table 5: List of components for the printed circuit board.

Component	Qty	Price
Op Amps	2	$3.300
G Connector	32	$4.096
P Connector	1	$0.129
R 100kΩ	16	$0.019
R 2kΩ	1	$0.001
R 1kΩ	9	$0.009
R 680Ω	1	$0.001
R 330Ω	40	$0.048
R 100Ω	32	$0.038
T 50Ω	32	$3.936
T 1kΩ	16	$1.024
C 0.16uF	10	$7.520
C 0.47uF	1	$0.026
C 100uF	1	$0.073
C 2.2uF	2	$0.016
C 10uF	2	$0.015
V. References	2	$6.580
MOSFET 40V	1	$0.546
Fuse 2A	1	$0.099
Regulator 9V	1	$3.350
Regulator 5V	1	$3.370
Rectifier diode	2	$3.370
LED	3	$0.014
STM32F407	1	$21.170
Schottky Diodes	8	$0.640
PCB Fabrication	1	$6.440
Header	4	$0.268

5 COMPARISON WITH COMMERCIAL DATA ACQUISITION SYSTEMS

In order to prove the effectiveness of the printed circuit board, several data acquisition boards composed by Wheatstone bridge circuits were analysed. The outstanding features are shown in Tab. 7. As it can be seen only two of them allow quarter, half or full bridge configurations which is a relevant characteristic depending of the force-torque sensor available to the user and using our PCB design we can reach any of these configurations. Moreover, only one has up to 16 Wheatstone bridge circuits, but its price is around ten times more expensive than our design. In relation with the amount of samples measured by second, four data acquisition boards reach up to 14400 but in our case we considered the STM32F407 Discovery which has analog to digital converters that can work in order of MHz (ST, 2022).

Table 6: List of components for the printed circuit board.

Component	Part number	Assembly
Op Amps	TLV9154QDRQ1	SMD
G Connector	JST XH-2	T-H
P Connector	Terminal Block 2 pin	T-H
R 100kΩ	WCR0805-100KFI	SMD
R 2kΩ	ERJ-6ENF2001V	SMD
R 1kΩ	ERJ-3EKF1001V	SMD
R 680Ω	ERJ-6ENF6200V	SMD
R 330Ω	ASC0805-330RFT5	SMD
R 100Ω	PCF0805R-100RBT1	SMD
T 50Ω	3224W	T-H
T 1kΩ	3224W	T-H
C 0.16uF	C0805C104Z4VACTU	SMD
C 0.47uF	885012207049	SMD
C 100uF	865080343009	SMD
C 2.2uF	885012107012	SMD
C 10uF	C2012JB1C106M085AC	SMD
V. References	MAX6018BEUR16+T	SMD
MOSFET 40V	DMP4047SK3-13	SMD
Fuse 2A	C1Q 2	SMD
Regulator 9V	R-78K9.0-1.0	T-H
Regulator 5V	mEZD71201A-G	T-H
Rectifier diode	FM4004W-W	SMD
LED	156120RS75300	SMD
STM32F407	STM32F407G-DISC1	T-H
Schottky Diodes	RB751S40T5G	SMD
PCB Fabrication	4 layers	-
Header	Connector	T-H

Table 7: Characteristics of Commercial Data Acquisition Boards (Windmill Software, 2015), (DATAQ Instruments, 2019),(DATAQ Instruments, 2014), (DATAQ Instruments, 2018), (Data Translation, 2017).

Data Acquisition Board	Bridge Type	Strain Gage Input Modules	ADC (samples /second per channel)	Price
DI-718Bx-S	Full bridge	6	14400	$1495
DI-4718B-U	Full bridge	6	14400	$695
DI-4718B-E	Full bridge	6	14400	$795
DI-718B-ES	Full bridge	6	14400	$895
DT9829-8	Quarter-bridge, Half-bridge, Full-bridge	8	120	$2159
751-SG	Quarter-bridge, Half-bridge, Full-bridge	16	48	$739.22

6 CONCLUSIONS

This paper proposed a low-cost printed circuit board which can be easily reconfigurable to work with different force-torque sensors based on strain gauges. Moreover it has an impedance control layer stackup to allow fast and reliable data transmission and other methods as ground stitching are employed to reduce electromagnetic interference. Besides, the components distributions were made in order to carry out a fast assembly process of SMD components using a pick-and-place machine and a solder oven. It is intended that this design can be useful to the user that requires a low cost system to measure forces in robotics applications.

ACKNOWLEDGEMENTS

This work has been supported by the Instituto de Investigaciones en Ingeniería as well as the School of Electrical Engineering from the University of Costa Rica.

REFERENCES

Aguirre-Ollinger, G. and Yu, H. (2021). Omnidirectional platforms for gait training: Admittance-shaping control for enhanced mobility. *Journal of Intelligent & Robotic Systems*, 101(3):52.

Armleder, S., Dean-Leon, E., Bergner, F., and Cheng, G. (2022). Interactive force control based on multimodal robot skin for physical human-robot collaboration. *Advanced Intelligent Systems*, 4(2):2100047.

Bussmann, K., Dietrich, A., and Ott, C. (2018). Whole-body impedance control for a planetary rover with robotic arm: Theory, control design, and experimental validation. In *2018 IEEE International Conference on Robotics and Automation (ICRA)*, pages 910–917.

Calanca, A., Muradore, R., and Fiorini, P. (2016). A review of algorithms for compliant control of stiff and fixed-compliance robots. *IEEE/ASME Transactions on Mechatronics*, 21(2):613–624.

Chen, D., Song, A., and Li, A. (2015). Design and calibration of a six-axis force/torque sensor with large measurement range used for the space manipulator. *Procedia Engineering*, 99:1164–1170. 2014 Asia-Pacific International Symposium on Aerospace Technology, APISAT2014 September 24-26, 2014 Shanghai, China.

Cheng, G., Dean-Leon, E., Bergner, F., Rogelio Guadarrama Olvera, J., Leboutet, Q., and Mittendorfer, P. (2019). A comprehensive realization of robot skin: Sensors, sensing, control, and applications. *Proceedings of the IEEE*, 107(10):2034–2051.

Circuits, S. (2020). High-speed pcb design guide. pages 30-32.

Data Translation (2017). Dt9828 usb multi-sensor measurement module. Datasheet. https://www.mccdaq.com/PDFs/specs/DT9829-Datasheet.pdf.

DATAQ Instruments (2014). Di-718b 8b module data logger system. Datasheet. https://www.dataq.com/resources/pdfs/datasheets/di718b_ds.pdf.

DATAQ Instruments (2018). Di-718bx 8b module data logger. Datasheet. https://www.dataq.com/resources/pdfs/datasheets/di718bx_ds.pdf.

DATAQ Instruments (2019). Di-4718b usb or ethernet data acquisition (daq) system. Datasheet. https://www.dataq.com/resources/pdfs/datasheets/di-4718b-data-logger-ds.pdf .

Dean, E., Ramirez-Amaro, K., Bergner, F., and Cheng, G. (2019). Robot skin: Fully-compliant control framework using multi-modal tactile events. *PÄDI Boletín Científico de Ciencias Básicas e Ingenierías del ICBI*, 7(Especial 1).

Dietrich, A., Bussmann, K., Petit, F., Kotyczka, P., Ott, C., Lohmann, B., and Albu-Schäffer, A. (2016). Whole-body impedance control of wheeled mobile manipulators. *Autonomous Robots*, 40(3):505–517.

Frémy, J., Ferland, F., Lauria, M., and Michaud, F. (2014). Force-guidance of a compliant omnidirectional nonholonomic platform. *Robotics and Autonomous Systems*, 62(4):579–590.

Iskandar, M., Quere, G., Hagengruber, A., Dietrich, A., and Vogel, J. (2019). Employing whole-body control in assistive robotics. In *2019 IEEE/RSJ International Conference on Intelligent Robots and Systems (IROS)*, pages 5643–5650.

JLCPCB (2023). Pcb manufacturing & assembly capabilities. https://jlcpcb.com/capabilities/pcb-capabilities. Last update on July 24, 2023.

Kebede, G. A., Ahmad, A. R., Lee, S.-C., and Lin, C.-Y. (2019). Decoupled six-axis force–moment sensor with a novel strain gauge arrangement and error reduction techniques. *Sensors*, 19(13).

Kim, K. S., Kwok, A. S., Thomas, G. C., and Sentis, L. (2014). Fully omnidirectional compliance in mobile robots via drive-torque sensor feedback. In *2014 IEEE/RSJ International Conference on Intelligent Robots and Systems*, pages 4757–4763.

Kim, K. S., Llado, T., and Sentis, L. (2016). Full-body collision detection and reaction with omnidirectional mobile platforms: a step towards safe human-robot interaction. *Autonomous Robots*, 40(2):325–341.

Kollmitz, M., Büscher, D., Schubert, T., and Burgard, W. (2018). Whole-body sensory concept for compliant mobile robots. In *2018 IEEE International Conference on Robotics and Automation (ICRA)*, pages 5429–5435.

Lin, C.-C., Su, C.-Y., Lin, S.-T., Chen, C.-Y., Yeh, C.-N., Lin, C.-H., Wang, L.-W., Kuo, S.-Y., and Chien, L.-J. (2019). 6-dof force/torque sensor. In *2019 14th International Microsystems, Packaging, Assembly and Circuits Technology Conference (IMPACT)*, pages 191–194.

Mittendorfer, P. a. G. (2012). 3d surface reconstruction for robotic body parts with artificial skins. In *2012 IEEE/RSJ International Conference on Intelligent Robots and Systems*, pages 4505–4510.

Nozawa, S., Ishida, M., Ueda, R., Kakiuchi, Y., Okada, K., and Inaba, M. (2011). Full-body motion control integrated with force error detection for wheelchair support. In *2011 11th IEEE-RAS International Conference on Humanoid Robots*, pages 193–198.

Oda, M., Zhu, C., Suzuki, M., Luo, X., Watanabe, H., and Yan, Y. (2010). Admittance based control of wheelchair typed omnidirectional robot for walking support and power assistance. In *19th International Symposium in Robot and Human Interactive Communication*, pages 159–164.

ONSEMI (2023). MOSFET Selection for Reverse Polarity Protection AND90146/D. https://www.onsemi.com/download/application-notes/pdf/and90146-d.pdf. Rev. 1.

Phan, T.-P., Chao, P. C.-P., Cai, J.-J., Wang, Y.-J., Wang, S.-C., and Wong, K. (2018). A novel 6-dof force/torque sensor for cobots and its calibration method. In *2018 IEEE International Conference on Applied System Invention (ICASI)*, pages 1228–1231.

Prabakaran, V., Elara, M. R., Pathmakumar, T., and Nansai, S. (2018). Floor cleaning robot with reconfigurable mechanism. *Automation in Construction*, 91:155–165.

Scrimizzi, F., Longo, G., and Gambino, G. (2016). Automotive-grade p-channel power mosfets for static, dynamic and repetitive reverse polarity protection. In *PCIM Europe 2016; International Exhibition and Conference for Power Electronics, Intelligent Motion, Renewable Energy and Energy Management*, pages 1–5.

Sentis, L., Petersen, J., and Philippsen, R. (2013). Implementation and stability analysis of prioritized whole-body compliant controllers on a wheeled humanoid robot in uneven terrains. *Autonomous Robots*, 35(4):301–319.

Singh, S., Singh, A., Singh, A., and Singh, S. (2019). Study on pcb designing problems and their solutions. In *2019 International Conference on Power Electronics, Control and Automation (ICPECA)*, page 4.

ST (2022). An2834 application note how to get the best adc accuracy in stm32 microcontrollers.

Sun, Y., Liu, Y., Jin, M., and Liu, H. (2013). Design and optimization of a novel six-axis force/torque sensor with good isotropy and high sensitivity. In *2013 IEEE International Conference on Robotics and Biomimetics (ROBIO)*, pages 631–638.

Templeman, J. O., Sheil, B. B., and Sun, T. (2020). Multi-axis force sensors: A state-of-the-art review. *Sensors and Actuators A: Physical*, 304:111772.

The Institute for Interconnecting and Packaging Electronic Circuits (1998). Ipc-2221: Generic standard on printed board design. pages 38,41-42.

Valizadeh, A., Akbarzadeh, A., and Heravi, M. H. T. (2015). Effect of structural design parameters of a six-axis force/torque sensor using full factorial design. In *2015 3rd RSI International Conference on Robotics and Mechatronics (ICROM)*, pages 789–793.

Windmill Software (2015). 751-sg user manual. Datasheet. https://www.windmill.co.uk/help/751sg.pdf.

Wong, C., Yang, E., Yan, X.-T., and Gu, D. (2018). Autonomous robots for harsh environments: a holistic overview of current solutions and ongoing challenges. *Systems Science & Control Engineering*, 6(1):213–219.

Yuan, C., Luo, L.-P., Yuan, Q., Wu, J., Yan, R.-J., Kim, H., Shin, K.-S., and Han, C.-S. (2015). Development and evaluation of a compact 6-axis force/moment sensor with a serial structure for the humanoid robot foot. *Measurement*, 70:110–122.

Zhang, M.-S., Mao, J.-F., and Long, Y.-L. (2011). Power noise suppression using power-and-ground via pairs in multilayered printed circuit boards. *IEEE Transactions on Components, Packaging and Manufacturing Technology*, 1(3):374–385.